

1 **Methodology to determine the coupling of continental clouds with surface [and](#)**
2 **[boundary layer height under cloudy conditions](#) from lidar and meteorological**
3 **data**

4
5 Tianning Su¹, Yutong ~~Zheng~~¹[Zheng](#)², and Zhanqing Li¹

6
7 ¹Department of Atmospheric and Oceanic Sciences & ESSIC, University of Maryland
8 , College Park, Maryland 20740, USA

9 [²The Program in Atmospheric and Oceanic Sciences, Princeton University, and](#)
10 [NOAA/Geophysical Fluid Dynamics Laboratory, Princeton, NJ, USA](#)

Formatted: Superscript

Formatted: Font: Calibri, Font color: Auto

Formatted: Normal, Left, Space Before: 0 pt, After: 0 pt,
Line spacing: single

11
12
13
14
15
16
17
18 *Correspondence to:* zhanqing@umd.edu; tianning@umd.edu

19 **Abstract**

20 The state of coupling between clouds and surface or boundary-layer have been
21 investigated much more extensively for marine stratocumulus clouds than for
22 continental low clouds, partly due to more complex thermodynamic structures over land.
23 A manifestation is a lack of robust remote sensing methods to identify coupled and
24 decoupled clouds over land. Here, we have generalized the concept of coupling and
25 decoupling to low clouds over land, based on potential temperature profiles.
26 Furthermore, by using ample measurements from a lidar and a suite of surface
27 meteorological instruments at the U.S. Department of Energy's Atmospheric Radiation
28 Measurement Program's Southern Great Plains site from 1998 to 2019, we have
29 developed a method to simultaneously retrieve the planetary boundary layer (PBL)
30 height (PBLH) and coupled states under cloudy conditions during the daytime. The
31 coupled states derived from lidar show strong consistency with those derived from
32 radiosondes. Retrieving the PBLH under cloudy conditions that has been a persistent
33 problem in lidar remote sensing, is resolved in this study. Our method can lead to high-
34 quality retrievals of the PBLH under cloudy conditions, and the determination of cloud
35 coupling states. With the new method, we find that coupled clouds are sensitive to
36 changes in the PBL, with a strong diurnal cycle whereas decoupled clouds and the PBL
37 are weakly related. Since coupled and decoupled clouds have distinct features, our new
38 method offers an advanced tool to separately investigate them in climate systems.

39 1 Introduction

40 A large fraction of low clouds is driven by surface fluxes through the conduits of
41 the planetary boundary layer (PBL) over land (e.g., Betts, 2009; Ek and Holtslag, 2004;
42 Golaz et al., 2002; Teixeira and Hogan, 2002; Zheng et al., 2020; Wei et al., 2020;
43 Santanello et al., 2018). This is a coupled cloud-surface system (Cheruy et al., 2014;
44 Zheng [&and](#) Rosenfeld, 2015; Wu et al., 1998). However, not all low clouds respond to
45 surface forcing. Those clouds without close interactions with the local surface are
46 considered to be in a decoupled state. Given that the PBL is, by definition, the lowest
47 atmospheric layer influenced by the underlying surface (Stull, 1988), to what degree
48 the PBL top overlaps with cloud bases becomes a good criterion to separate coupled
49 and decoupled low clouds.

50 Conventionally, the “coupled state” of a cloud-topped marine boundary layer
51 implies that the moist conserved variables are vertically well mixed within the PBL
52 (Bretherton and Wyant, 1997; Dong et al., 2015; Zheng [&and](#) Li, 2019; Zheng et al.,
53 2018). However, such a definition cannot be simply applied to clouds over land since
54 the moist conserved variables typically show considerable variations due to the
55 relatively complex thermodynamics (Driedonks, 1982; Stull, 1988). The definition and
56 the determination methods of the PBL over land also widely differ from those over
57 ocean (Garratt, 1994; Vogelesang [&and](#) Holtslag, 1996). The concept of coupled and
58 decoupled states is typically used to characterize marine stratocumulus clouds due to
59 their large-scale coverages (Nicholls, 1984). Since stratocumulus only constitutes a
60 relatively small portion of continental clouds (Warren et al., 1986), we attempt to extend

61 the concept of coupling and decoupling to characterize low clouds over land.

62 Following parcel theory, the lifted condensation level (LCL) has been used to
63 diagnose a coupled cloud, based on the distance between the LCL and the cloud base
64 (e.g., Dong et al., 2015; Glenn et al., 2020; Zheng [and](#) Rosenfeld, 2015; Zheng et al.,
65 2020). When potential temperature and humidity are uniformly distributed in the
66 vertical, the LCL should be consistent with the cloud base for coupled cases. However,
67 the cloud base for coupled cases can considerably differ from the LCL over land
68 because potential temperature and humidity have large variabilities in the vertical scale
69 within the PBL over land (Guo et al., 2016; Stull, 1988; Su et al., 2017a). Therefore, a
70 robust remote sensing method is still warranted to distinguish coupled and decoupled
71 clouds over land.

72 Since the PBL height (PBLH) is the maximum height directly influenced by surface
73 fluxes, we consider coupling with the PBL equivalent to coupling with the land surface.
74 Thus, we use the PBLH as a critical parameter to diagnose the coupling between clouds
75 and the land surface. The degree of coupling may thus be gauged in terms of
76 quantitative differences between the cloud base and the PBL top. Such differences can
77 be determined in a height coordinate system or in a potential temperature coordinate
78 system (Kasahara, 1974). For this purpose, ground-based lidar has great potential
79 because it can continuously track the development of the PBL (Demos et al., 2006;
80 Hageli et al., 2000; Sawyer [and](#) Li, 2013; Su et al., 2017b) and clouds (Clothiaux et
81 al., 2000; Platt et al., 1994; Zhao et al., 2014) at high temporal and vertical resolutions.

82 By jointly using lidar measurements and meteorological data from the U.S.

83 Department of Energy’s Atmospheric Radiation Measurement (ARM) Southern Great
84 Plains (SGP) site (36.6°N, 97.48°W), we attempt to identify coupled and decoupled low
85 clouds during the daytime. Unlike previous studies that use the LCL or radiosonde (RS)
86 data to diagnose coupled clouds (e.g., Dong et al., 2015; Zheng [and](#) Rosenfeld, 2015),
87 this study provides the first lidar-based method to automatically determine the coupling
88 and decoupling of low clouds over land at a high temporal resolution.

89 The paper is organized as follows. Section 2 describes the measurements and data.
90 Section 3 describes the new methodology in terms of the definition and implementation.
91 The performance of the method is demonstrated in Section 4, and a summary is
92 presented in Section 5.

93

94 **2 Data Descriptions**

95 *2.1 Radiosonde*

96 RS launches took place at least four times per day at the ARM SGP site, usually at
97 0030, 0630, 1230, and 1830 local time (LT). Holdridge et al. (2011) provide technical
98 details about the ARM RS (<https://www.arm.gov/capabilities/instruments/sonde>). In
99 this study, we consistently use daylight saving time (Coordinated Universal Time -5 h)
100 as local time throughout the year to avoid inconsistencies between summer and winter.
101 Besides the routine measurements, there are fewer, but still considerable numbers of
102 RS data obtained at other times of the day (e.g., 0930, 1200, 1300, 1530, and 1900 LT).
103 These supplemental RS samples at other times comprise ~10% of the total number of

104 cases. RS data from 0630–1900 LT are utilized in this study. The vertical resolution of
105 RS data varies according to the rising rate of the balloon, but measurements are
106 generally taken ~10 m apart. We further vertically average the RS data to achieve a
107 vertical resolution of 5 hPa.

108 There are several methods to determine PBLH from RS-measured temperature,
109 pressure, and humidity profiles. ~~These methods include, among others, the parcel~~
110 method (Holzworth, 1964), ~~the~~ gradient methods (Stull, 1988; Seidel et al., 2010), and
111 the Richardson number method (Vogelezang and Holtslag, 1996). ~~After~~
112 ~~examining~~Based on the previous methods, Liu and Liang (2010) ~~use~~proposed a
113 different ~~strategies~~approach to determine the PBLH that is valid under different
114 thermodynamics ~~stability~~ conditions. ~~The~~ ~~As this method demonstrates~~ ~~r~~Robust
115 performance was demonstrated over the SGP site and in other major field campaign
116 sites ~~its~~around the world (Liu and Liang, 2010). Thus, we adopted this method ~~which~~
117 ~~was thus chosen~~to calculate PBLH from RS data in ~~our~~this study. ~~By using the well-~~
118 ~~established method developed by Liu and Liang (2010), we retrieved PBLHs over the~~
119 ~~SGP site from RS measurements.~~ The potential temperature is corrected as the virtual
120 potential temperature, θ_v , using the water vapor mixing ratio [WVMR; $\theta_v = (1 +$
121 $0.61\text{WVMR})$]. The virtual potential temperature does not include a correction for the
122 liquid water content profile, as this is challenging to measure in many conditions.
123 Therefore, the virtual potential temperature is not conserved during moist convection.
124 Since we mainly focus on the sub-cloud atmosphere, this is not a serious problem.
125 Moreover, we use scaled RS moisture profiles normalized by the total precipitable

Formatted: Font: Not Bold

126 water vapor derived from the microwave radiometer
127 (<https://www.arm.gov/capabilities/vaps/lssonde>, Revercomb et al., 2003).

128

129 *2.2 Micropulse lidar (MPL) system*

130 MPL backscatter profiles were collected at the SGP site from September 1998 to
131 July 2019 with high continuity (Campbell et al., 2002). Technical details and data
132 availability can be found at the website
133 <https://www.arm.gov/capabilities/instruments/mpl>. The backscatter profiles have a
134 vertical resolution of 30 m. MPL signals have an initial temporal resolution of 10–30 s
135 and are averaged every 10 min for this study. Due to the inherent problem of lidar
136 observations, there is a ~0.2-km near-surface “blind zone”. Following the standard
137 lidar-data processing, background subtraction, signal saturation and overlapping, after-
138 pulse and range corrections are applied to the raw MPL data (Campbell et al., 2002,
139 2003). Questionable data are excluded based on the quality-control flags.

140

141 *2.3 Cloud product*

142 The MPL can be used to detect cloud layers based on signal gradients (Platt et al.,
143 1994). Lidar-based methods are accurate for determining the cloud-base height (CBH)
144 but may miss information about the cloud top due to the signal saturation within an
145 optically thick cloud (Clothiaux et al., 2000). Under this condition, the cloud radar
146 provides a better estimation of the cloud-top height (CTH). In this study, we directly

147 use an existing quality-controlled cloud product, CLDTYPE/ARSCL
148 (<https://www.arm.gov/capabilities/vaps/cldtype>), which combines information from
149 the MPL, ceilometer, and cloud radar to determine the vertical boundaries of clouds
150 (Clothiaux et al., 2000; Flynn et al., 2017). For the lowest cloud base, the best
151 estimation from laser-based techniques (i.e., MPL and ceilometer) is used. The original
152 temporal resolution of the CLDTYPE/ARSCL product is 1 min, averaged to a 10-min
153 temporal resolution. To avoid averaging jumps in signal between different clouds, a
154 cloud is considered to be continuous if its base height varies less than 0.25 km between
155 two consecutive profiles.

156

157 **3 Methodology**

158 *3.1 Definition of coupled and decoupled clouds based on thermodynamics*

159 The definition of the state of cloud-surface coupling over land is a critical question.
160 For marine stratocumulus, coupled clouds are identified when the liquid water potential
161 temperature varies less than a certain threshold (i.e., 0.5 K) below the cloud base (Jones
162 et al., 2011). We try to extend the concept of coupling and decoupling to clouds over
163 land. The PBL over land is typically buoyancy driven and controlled by surface fluxes
164 during the daytime. We consider a cloud is in the coupled state when it strongly interacts
165 with the buoyancy fluxes within the PBL.

166 Figure 1 presents the idealized vertical profiles of virtual potential temperature (θ_v)
167 under the clear-sky, coupled cloud, and decoupled cloud. A superadiabatic surface layer

168 exchanges the heat fluxes between the surface and PBL. The outer layer and
169 entrainment zone are turbulently coupled with the surface, and thus, are considered as
170 the coupled regime. Meanwhile, the free atmosphere is considered as the decoupled
171 regime. Theoretically, θ_v is constant in the outer layer, and follows the wet adiabatic
172 lapse rate in the cloud layer. Although the profiles of θ_v in the real atmosphere can
173 largely differ from the idealized profiles, the relative position between the cloud layer
174 and capping inversion of entrainment zone is clear. For the coupled cases, the cloud
175 base is below the capping inversion of entrainment zone. For the decoupled cases, the
176 cloud base is above the capping inversion. Based on this feature, we can use the virtual
177 potential temperature profiles to diagnose the coupling state of low clouds.

178 We first look at several examples of profiles of θ_v and WVMR from the RS
179 (Figure 2). If the CBH is lower than the PBLH, the cloud is affected by turbulence and
180 buoyancy fluxes in the PBL, such as the cases shown in Figure 2a. Note that the PBLH
181 is not an absolute boundary limiting turbulence and buoyancy fluxes. Due to the
182 overshooting of rising air parcels, we use a range to screen the condition of coupled
183 clouds. As shown in Figure 2b, even when the CBH is slightly above the PBLH,
184 WVMR and θ_v are still relatively consistent between the cloud layer and the PBL and
185 show large step signals at the cloud top.

186 Figure 2c-d shows a clear inversion layer between the cloud base and the PBL top,
187 and the difference in θ_v between the CBH and the PBLH ($\Delta\theta_v$) is relatively large.
188 Such a notable inversion layer prevents the buoyancy fluxes within the PBL from
189 reaching the cloud base, leading to the decoupling between the cloud and the PBL.

190 Overall, whether there is a clear inversion between the cloud base and the PBL top is
191 the key factor in determining coupling and decoupling. In this aspect, $\Delta\theta_v$ is the key
192 factor. In Figure 2, $\Delta\theta_v$ for coupled cases (a-c) is -0.32 K and 0.31 K, respectively,
193 and $\Delta\theta_v$ for decoupled cases (d-e) is 1.47 K and 5.0 K, respectively.

194 Therefore, instead of giving a height range to limit the differences between CBH
195 and PBLH, we consider using the differences in θ_v between CBH and PBLH ($\Delta\theta_v =$
196 $\theta_v^{\text{CBH}} - \theta_v^{\text{PBLH}}$) to determine the threshold for distinguishing coupled and decoupled
197 clouds. For convenience, we use $\Delta\theta_v$ to refer to the difference in θ_v between the
198 CBH and the PBLH ($\Delta\theta_v = \theta_v^{\text{CBH}} - \theta_v^{\text{PBLH}}$). For decoupled cases, the cloud base is
199 above the capping inversion of entrainment zone. There is a notable inversion in θ_v
200 between PBL top and decoupled cloud base. Thus, we identify the cases satisfying
201 $\Delta\theta_v > \delta_s$ as being in a decoupled state. Correspondingly, we identify the cases
202 satisfying $\Delta\theta_v < \delta_s$ as being in a coupled state. We set the range of CBH to between
203 0 and 4 km and excluded cases of deep convection (i.e., $\text{CBH} < 4$ km and $\text{CTH} > 6.5$
204 km).

205 As the basic framework of PBL, the slab model assumes that θ_v is constant within
206 the PBL (Wallace and Hobbs, 2006). Under this assumption, δ_s can be set as 0.
207 However, there are certain variations in θ_v within the PBL, which can cause inversions
208 with relatively small magnitudes between the cloud base and PBL top. Figure 3a
209 presents the inversion strength in θ_v within PBL during the daytime. Specifically,
210 inversions represent the layers with continuously increased structures of θ_v . For an
211 inversion layer, the inversion strength is calculated as the differences in θ_v between the

Formatted: Normal, Left, Space Before: 6 pt, Pattern: Clear

Formatted: Font: Not Bold

Formatted: Font: Not Bold

Formatted: Font: Not Bold

Formatted: Font: Not Bold

Formatted: Font: Not Bold

Formatted: Font: Not Bold

Formatted: Font: Not Bold

212 ~~layer top and bottom of the layer.~~ The inversions near surface or across the PBL top are
213 excluded. Besides the capping inversion and surface inversion, the inversion strength
214 within PBL is typically below 1K. Therefore, we set δ_s as 1 K, which is the same as
215 the criterion for determining stable or convective conditions (Liu ~~&~~ Liang, 2010).
216 Furthermore, we demonstrate the probability density function (PDF) of $\Delta\theta_v$ for the
217 low cloud cases. Coupled and decoupled clouds are classified by the threshold of δ_s
218 (1 K). Through the development of PBL, boundary layer clouds frequently occur in the
219 entrainment zone, and form a coupled cloud-PBL system. For such coupled systems,
220 θ_v at cloud top and PBL top is highly consistent for the majority of cases. Thus, the
221 PDF of $\Delta\theta_v$ shows significantly high values for the range of -2 K to 0.5 K in the
222 coupled regime. Meanwhile, the PDF of $\Delta\theta_v$ is evenly distributed in the decoupled
223 regime. Since we only analyze low clouds, the PDF of $\Delta\theta_v$ slowly decrease when $\Delta\theta_v$
224 is above 10 K.

Formatted: Font: Not Bold

Formatted: Font: (Asian) Times New Roman, Bold, Font color: Black

225 Based on the variations in θ_v within PBL, we set δ_s as 1 K. However, it should
226 note that it is not an absolute value. A similar threshold of 0.5 K has been used for
227 marine stratocumulus (Jones et al., 2011; Dong et al., 2015). Comparing to the marine
228 condition, θ_v show greater variabilities over land. Hence, the threshold is
229 correspondingly larger. On the other hand, since the threshold of 1 K is in the low PDF
230 regime (Figure 3b), the small changes in this value would not notably affect the
231 identifications. Specifically, a 0.1 K difference in δ_s will lead to a 0.5% difference in
232 the identification of coupled cloud.

Formatted: Indent: First line: 0.29", Space Before: 0.3 line

233 Same to the previous studies (Jones et al., 2010; Dong et al., 2015; Zheng and

234 Rosenfeld, 2015), ~~our study~~we identified the coupled clouds as the thermodynamics
235 coupling between surface and cloud base. However, it is an open question whether the
236 entire cloud layer is coupled for coupled cases. It depends on whether the liquid water
237 potential temperature is conserved within the cloud layer, which represents ~~the~~
238 moisture adiabatic process. This issue is closely related to the cloud types. In the cloud
239 parameterizations, the entire stratocumulus layer is considered to be well-mixed,
240 ~~meanwhile~~; the cumulus-capped layer is usually partially mixed (Lock, 2000). ~~For~~
241 stratocumulus clouds, the entire cloud layer and PBL are typically fully coupled with
242 surface, when the cloud base is coupled with surface. For the cumulus-capped PBL, the
243 entire cloud layer may not be completely coupled, despite the coupling between cloud
244 base and surface. ~~For stratocumulus clouds, may. Foreclouds, they are~~The well-
245 established parameterizations ~~also~~ are supported by many observational studies (e.g.,
246 Betts, 1986; Storer et al., 2015; Berkes et al., 2016, de Roode and Wang, 2006; Ott et
247 al., 2009).

Formatted: Font: Not Bold

Formatted: Font: Not Bold

Formatted: Indent: First line: 0"

248
249 Following the traditional definition of buoyancy forces (Wallace & Hobbs, 2006), we
250 further integrate the buoyancy forces within the lowest 1 km ($-g \int_0^{1\text{km}} \frac{\Delta\theta}{\theta} dz$). Figure
251 4 shows the relationships between CBH and buoyancy forces in the lower atmosphere
252 for $-\Delta\theta_p < \delta_p$ (coupled state) and $-\Delta\theta_p > \delta_p$ (decoupled state). In terms of the
253 responses to buoyancy forces, dramatic differences between coupled and decoupled
254 clouds are seen. Following our previous study (Su et al., 2018), we use the inverse
255 fitting ($f(x) = \frac{A}{x} + B$) with consideration of density to establish the relationship

256 between CBH and buoyancy forces. The magnitude of the correlation coefficient (R^{\pm})
257 is designed to measure the degree to which the data fit an inverse relationship. For a
258 coupled cloud, changes in CBH to variable buoyancy forces mostly follow an inverse
259 function. For the coupled cases, strong buoyancy forces are associated with a thick PBL
260 and high CBH. Since a decoupled cloud occurs in the free atmosphere, the CBH of a
261 decoupled cloud has a very weak linkage with the buoyancy forces.

262

263 3.2 Lidar-based method to identify coupled and decoupled clouds

264 3.2.1 Method description

265 Given the rapid change in clouds over land, RS observations have limitations when
266 it comes to tracking cloud development due to the coarse temporal resolution and
267 drifting of the balloon. We thus further developed a lidar-based method to identify the
268 coupled states of clouds based on our new algorithm for retrieving the PBLH that can
269 better track the diurnal variations in PBLH than conventional lidar-based approaches
270 (Su et al., 2020). We adapted this algorithm for retrieving the PBLH and developed a
271 new scheme to deal with cloudy conditions. Following the original method (Su et al.
272 2020), the rainy cases are eliminated in the quality control process. ~~As stated in Su et~~
273 ~~al. (2020), the rainy cases are eliminated in the quality control process.~~ The principles
274 behind the PBLH algorithm are stated next for completeness.

275 Our new PBLH algorithm can retrieve the PBL variability from the MPL under
276 Different Thermo-Dynamic Stability (thus named the DTDS algorithm) conditions,

Formatted: Font: Not Bold

277 taking into account the vertical coherence and temporal continuity of the PBLH. First,
278 we identify the local maximum positions (LMPs; range: 0.25–4 km) in profiles of the
279 wavelet covariance transform function derived from lidar backscatter (Brooks, 2003).
280 These LMPs are the potential positions of the PBLH. We can use the PBLH derived
281 from morning RS soundings as the starting point. Without morning RS soundings, the
282 algorithm can still work well, with the lowest LMPs selected as the starting point, which
283 reduces by 0.02–0.05 the correlation coefficient between MPL-derived and RS-derived
284 PBLHs (Su et al., 2020).

285 To ensure good continuity, we select the closest LMP to the earlier position of the
286 PBLH. Different stages of PBL development are considered. DTDS-derived PBLHs
287 likely increase during the growth stage and decrease during the decaying stage, but the
288 algorithm is also able to identify decreases during the growth stage or increases during
289 the decaying stage based on the selection scheme described by Su et al. (2020). There
290 are multiple step signals in the backscatter profiles when complex aerosol structures
291 (e.g., the residual layer) are present, leading to multiple LMPs. Based on temporal
292 continuity, we select the appropriate LMP as the position of the PBL top. However,
293 PBLH retrievals still suffer from relatively low accuracies under stable conditions
294 because of the weak vertical mixing and residual layer.

295 Clouds induce strong step signals in the lidar backscatter, further considerably
296 affecting PBLH retrievals. Su et al. (2020) only considered cases where the low cloud
297 top coincided with the previous PBL top, excluding other low-cloud cases (> 60% of
298 all low-cloud cases). Here, we specifically consider coupled and decoupled states of

299 low clouds. Due to the MPL's ~0.2-km blind zone, we only analyze the PBLH and CBH
300 above 0.2 km. Figure 5-4 presents the flow chart describing the updated DTDS
301 algorithm. In particular, we jointly use PBL development and the LCL to diagnose the
302 states of coupling or decoupling. In ideal situations, LCL, PBLH, and CBH are highly
303 consistent with each other for coupled clouds. But for real conditions, we only require
304 that either the LCL or the PBLH coincides with the CBH for identifying coupled cases,
305 with another parameter serving as an additional constraint. Specifically, a coupled cloud
306 needs to occur within a certain range of LCL and the previous position of the PBL top.

307 For the DTDS algorithm, five empirical parameters are used, including A_1 , A_2 ,
308 A_3 , A_4 , A_5 . As listed in the Table 1, $A_1 - A_5$ are set as 0.7, 0.2, 0.15, 1.35, and 1.1,
309 respectively. A cloud at time i is identified as being in the coupled state if the CBH is
310 less than $[H(i - 1) + 0.2 \text{ km } (A_2)]$ and $[LCL + 0.7 \text{ km } (A_1)]$. This step would
311 moves 39.5% of low cloud cases to the category of decoupled clouds. A cloud is also
312 considered to be in a coupled state if the CBH is coincident with the LCL within 0.15
313 km (A_3), and the CBH is less than $[H(i - 1) + 0.7 \text{ km } (A_1)]$, where $H(i - 1)$
314 represents the PBLH at time $(i - 1)$. This step would further moves 17.8% of the
315 remaining cases to the category of decoupled clouds.

316 The LCL is calculated from surface meteorological data (relative humidity,
317 temperature, pressure) at the SGP site based on an exact expression (Romps, 2017).
318 Specifically, Romps. (2017) proposed the exact, explicit, analytic expression for LCL
319 as a function of surface meteorology. Compared to the previous approximate
320 expressions, some of which may have an uncertainty of in the order of hundreds of

Formatted: Space Before: 6 pt

Formatted: Font: Not Bold

Formatted: Font: Not Bold

Formatted: Font: Not Bold

Formatted: Font: Not Bold

Formatted: Font: Not Bold

Formatted: Font: Not Bold

Formatted: Default Paragraph Font, Font: Times New Roman, 12 pt, Font color: Auto

Formatted: Default Paragraph Font, Font: Times New Roman, 12 pt, Font color: Auto

Formatted: Default Paragraph Font, Font: Times New Roman, 12 pt, Font color: Auto

Formatted: Default Paragraph Font, Font: Times New Roman, 12 pt, Font color: Auto

Formatted: Default Paragraph Font, Font: Times New Roman, 12 pt, Font color: Auto

321 meters, for which, the Romps expression can be considered as the precise value. The
322 uncertainty of empirical vapor pressure data may lead to a bias of ~5-m (Romps, 2017),
323 which may be neglected in the analyses.

324 After determining the coupling or decoupling state of a cloud, we retrieve $H(i)$
325 (i.e., PBLH at time i) based on the cloud state. For decoupled cases, we use the same
326 strategy for a clear sky to retrieve the PBLH. Based on the selection scheme in the
327 DTDS algorithm, the LMP below the CBH is selected as $H(i)$. For coupled cases, we
328 jointly use CBH and CTH to determine PBLH. During the warm season, active cumulus
329 often occurs in the upper part of the PBL with strong surface heating, so the CBH can
330 be generally regarded as the PBLH (Stull, 1988; Wallace & Hobbs, 2006). Under
331 this condition, the CBH coincides with the previous PBL top. Therefore, if $[CTH \geq$
332 $PBLH_{30min} + 0.2 \text{ km } (A_2)]$, we set $H(i) = A_5CBH$, where $PBLH_{30min}$ is the
333 average value of the PBLH within 30 min of the prior time i . Hence, A_5 would be a
334 critical parameter for the PBLH estimation. On the other hand, if $[CTH <$
335 $PBLH_{30min} + 0.2 \text{ km } (A_2)]$. we set $H(i)$ equal to the minimum between CTH and
336 the product A_4*CBH . This step is designed for thin clouds or some stratiform clouds.
337 In particular, A_5*CBH can be notably larger than the CTH for a thin cloud. Under this
338 situation, we tend to use CTH to ~~represent~~denote the PBL top. This step has little impact
339 on the detection of surface-cloud coupling, but can assure that the CTH of the coupled
340 cloud is always higher than the retrieved PBLH to fit the real situation.

Formatted: Font: (Asian) Times New Roman, Font color: Black

341 –After retrieving $H(i)$, we consider that the cloud above the PBLH is still coupled
342 if $[CBH < H(i) + 0.2 \text{ km } (A_2)]$. Moreover, we added an upper limit for all PBLH

343 retrievals. If $[H(i) > LCL + 0.7 \text{ km } (A_1)]$, we adjust $H(i)$ as the maximum LMP
344 below the LCL. The new DTDS method combines lidar measurements and surface
345 meteorological observations and can simultaneously retrieve the PBLH and cloud states.
346

347 3.2.2 Selection of empirical parameters

348 The states of coupling and decoupling are diagnostic parameters rather than explicit
349 expressions. Similar to the other methods for retrieving PBLH (e.g., Brooks, 2003; Liu
350 [and Liang, 2010](#)), multiple empirical parameters are used to determine PBLH. Here
351 we discuss the selection of empirical parameters in the algorithm.

352 Note that we used the CTH and $A_4 * CBH$ as the upper limits for PBLH retrievals in
353 the DTDS algorithm. For coupled cases, these two limits are generally close to or above
354 the position of the PBL top. Only 2% (3%) of total cases meet the condition that the
355 RS-derived PBLH is 0.25 km higher than the CTH ($A_4 * CBH$). Section 4 presents the
356 detailed relationships between CBH, CTH, and PBLH. In the DTDS method, CTH
357 serves as the upper limit for PBLH under the condition of coupled shallow cumulus.

358 Similar to previous studies, we can also use the LCL as the standard to identify
359 coupled clouds (Dong et al., 2015; Zheng [and Rosenfeld, 2015](#)). We assume a cloud
360 is coupled if $|CBH - LCL| < \Delta h$ ~~some criteria~~. [By using ~7500 RS profiles, the cloud](#)
361 [coupling state derived from the virtual potential temperature method \(Section 3.1\) is](#)
362 [considered as the ground truth for evaluation](#). Figure ~~6a~~ [5a](#) shows the commission errors
363 and omission errors for different criteria. Here, the commission error is calculated as

Formatted: Font: Not Bold

364 the percentage of decoupled clouds misidentified as coupled clouds. The commission
365 error can also be called a “false positive”, as the former is a common term for describing
366 the nature of an error in identification. The omission error is calculated as the
367 percentage of coupled clouds that have not been identified under this criterion. By using
368 the LCL, we can obtain a relatively low commission error if the criterion is less than
369 0.15 km and a relatively low omission error if the criterion is greater than 0.7 km. Thus,
370 we set A_1 and A_3 as 0.7 and 0.15 in the DTDS method to exclude and to select cases
371 of coupled clouds. We can also use the RS-derived PBLH as the criterion (Figure 6b5b).

372 Despite the coarse temporal resolution, the RS-derived PBLH can be a good
373 criterion to use to distinguish between coupling and decoupling. If we consider a
374 coupled cloud as a cloud where ($CBH < RS\text{-derived PBLH} + 0.2 \text{ km}$), both commission
375 and omission errors are ~5%. Therefore, we primarily use $[PBLH + 0.2 \text{ km} (A_2)]$ in the
376 DTDS method to identify coupled and decoupled regimes. As cloud can considerably
377 interfere affect with lidar backscattering and generate large signal variations, we jointly
378 use lidar backscatterings, the previous position of PBL top, and LCL to determine the
379 surface-cloud coupling and PBLH. In particular, the LCL constraint in the algorithm
380 notably reduces the absolute biases in PBLH retrievals under cloudy conditions by 9.3%.

381
382
383 Moreover, we test the sensitivity of selecting these empirical parameters. Figure 7
384 6 presents the commission errors and omission errors in the identifications of coupled
385 clouds for selecting different values of empirical parameters. Among these parameters,

Formatted: Font: Not Bold

Formatted: Font: Not Bold

Formatted: Font: Not Bold

Formatted: Font: Not Bold

Formatted: Font: Not Bold

Formatted: Font: Not Bold

Formatted: Indent: First line: 0.25"

386 A_2 is the critical one, which would notably affect the identification results. In general,
387 A_2 determine the maximum differences between PBLH and CBH for coupled cases. If
388 $[CBH-PBLH > A_2]$, we consider the cloud is under the decoupled state. Thus, the
389 identification method is quite sensitive to A_2 . Selecting a low value of A_2 would
390 neglect many coupled cases, which leads to a high omission error. Meanwhile, selecting
391 a high value of A_2 would misclassify many coupled cases, which leads to a high
392 commission error. After a trail and error, A_2 is set as 0.2 km to balance the omission
393 and commission errors. The selections for other parameters are not sensitive for the
394 coupled cloud identifications. We can choose them from a reasonable range.

395 As a by-product of this method, we also pay attentions to the PBLH retrievals under
396 cloudy conditions. Figure 8-7 presents the mean absolute biases and correlation
397 coefficients between PBLH derived from lidar and radiosonde for selecting different
398 values of empirical parameters. To match the scope of this study, we only analyze the
399 low cloud conditions. For retrieving PBLH under cloudy conditions, A_2 is the critical
400 parameter. The variations in correlation coefficients under different values of empirical
401 parameters are small with a range of 0.81-0.82. However, the absolute biases can
402 considerably differ under different values of A_5 . In general, A_5 represents the ratio
403 between CBH and PBLH under coupled conditions. If A_5 is above 1.1, PBLH
404 retrievals under cloudy conditions are overestimated. We set A_5 as 1.1 to achieve a
405 ~~relatively low bias~~ ~~relatively low biases~~ and a relatively high correlation coefficient at
406 the same time. For other parameters, the selections from reasonable ranges would not
407 notably affect the PBLH retrievals.

408 In short, selections of these empirical parameters are based on the overall
409 relationship between cloud and PBL under the coupled and decoupled states. In our
410 method, the selection of A_2 is critical for the identifications of coupled clouds, while
411 the selection of A_5 is critical for the PBLH retrievals under cloudy conditions. The
412 selections of other parameters are not sensitive.

413

414 4 Results

415 ~~Figure 9~~ ~~Figure 8~~ illustrates four examples of PBLH retrievals and cloud states
416 derived from the DTDS algorithm for 27 October 2011, 31 July 2002, 19 March 2000,
417 and 1 May 2012. ~~Figure 9a~~ ~~Figure 8a~~ depicts coupled shallow cumulus occurring at
418 noontime at the PBL top. With a weak surface flux of $\sim 200 \text{ W m}^{-2}$, this shallow cumulus
419 cloud appeared for less than an hour. Figure ~~9b~~ ~~8b~~ shows a developed coupled cumulus
420 cloud. With a strong surface flux of $\sim 500 \text{ W m}^{-2}$, this coupled cloud continuously
421 developed during the daytime. Figure ~~9c~~ ~~8c~~ presents the case of a daylong coupled
422 cloud. After the passage of a frontal system that day, stratocumulus occurred during the
423 morning with a cloud thickness of 0.5 km. Through the development of the PBL, the
424 thick stratocumulus cloud was broken up by the strong turbulences, transforming into
425 shallow cumulus clouds. Figure ~~9d~~ ~~8d~~ shows the case of an active coupled cloud, which
426 is generally associated with a large amount of convective available potential energy.
427 Even though coupled clouds can differ in appearance and variability throughout the day,
428 the common feature is the coherent variation between the cloud base and the PBL top.

429 The LCL is a relevant parameter and can differ from the PBLH and the CBH for some
430 coupled cases (e.g., Figure 9b8b-c).

431 The identification accuracy, or disparity between different methods, are evaluated
432 in terms of the selected criteria, for which the identification method based on $\Delta\theta_v$ is
433 regarded as the “truth”, as described in Section 3.1. Hereafter, all results are analyzed
434 for the period of 1000–1900 LT, so early-morning data are not used. The commission
435 error is 10.1%, and the omission error is 6.8% for the DTDS method. Note that lidar-
436 based PBLH methods generally suffer from relatively low accuracy under stable
437 atmospheric conditions. Following Liu and Liang (2010), we identified stable PBLs
438 from RS measurements. Since coupled clouds are driven by relatively strong buoyancy
439 fluxes, only 1% of total cases of coupled clouds occurred under stable PBL conditions
440 during the study period (0700–1900 LT). Therefore, the relatively low accuracy for
441 stable PBLs is not a major problem in this study.

442 Figure 6-5 also compares the accuracy between the DTDS and LCL methods. Based
443 on the LCL alone, we cannot choose an appropriate criterion to achieve a lower
444 commission error and omission error simultaneously. Thus, we do not use the LCL as
445 the single standard to detect the coupling and decoupling of low clouds in our study. As
446 diagnostic parameters, different methods inevitably produce different results regarding
447 coupling and decoupling. Although we consider the method based on $\Delta\theta_v$ as the
448 standard, it still suffers from uncertainties arising from balloon drifting. From this
449 perspective, it is hard to conclude which method is the best. Since it determines the
450 PBLH based on aerosol backscattering, the lidar-based method may be more

451 representative of the coupling between a cloud and the aerosol layer near the surface
452 when clear skies occur, at least during a short window of time.

453 Figure 10a2a-b presents the occurrence frequencies of the CBH and the CTH at
454 different heights. Despite the same variation ranges, clouds are mostly coupled if the
455 CBH is lower than 1 km, while decoupled clouds dominate if the CBH is higher than 3
456 km. Figure 10e9c-d shows the changes in the coupled fraction (ratio of coupled cases
457 to total cases) with different CBHs and CTHs. The coupled fraction is about 90% if the
458 CBH is lower than 1 km and decreases to 2% for CBHs above 3 km. Although the CBHs
459 for coupled cases are generally less than 3 km, CTHs for coupled cases can be much
460 higher. Coupled clouds still account for around 10% of the cases with CTHs above 6
461 km.

462 Figure 11-10 shows scatter plots between CBH, CTH, PBLH, and LCL for coupled
463 and decoupled clouds. For coupled clouds, there is a generally strong correlation
464 between CBH, LCL, and PBLH, contrary to the weak relationships of decoupled cases.
465 The relationship between CTH and RS-derived PBLH is complicated. For shallow
466 cumulus clouds, their tops can be considered as PBL tops for the coupled state, while
467 the cloud top is considerably above the position of the PBL top for active cumulus
468 clouds. We also note that the accuracy of CTH retrievals is generally lower than the
469 accuracy of CBH retrievals (Clothiaux et al., 2000). As CTH is not a criterion for cloud
470 coupling, the accuracy of CTH would not affect the identification of coupled cloud, but
471 may affect the PBLH retrievals for the coupled cloud cases. Meanwhile, despite the
472 laser-based detection of CBH is considered as the standard method (Platt et al., 1994;

Formatted: Indent: First line: 0.29", Space Before: 6 pt

Formatted: Font: Not Bold

473 [Clothiaux et al., 2000; Lim et al., 2019](#)), the CBH retrievals from ceilometer or lidar
474 [still bear some uncertainties, which can potentially lead to a mean bias of 0.1km \(Silber](#)
475 [et al., 2018; Cromwell et a., 2019\)](#). In our method, a systematic increase of 0.1 km in
476 [the CBH can lead to an increase of 2.1% in omission errors and a decrease of 1% in](#)
477 [commission errors.](#)

478 After identifying the coupling ~~or decoupling~~state of clouds, [it is feasible to retrieve](#)
479 ~~the PBLH under cloudy conditions~~[the PBLH can be successfully retrieved under cloudy](#)
480 ~~conditions. In particular, the DTDS-derived PBLH needs to resort to the cloud position~~
481 ~~for coupled cloud cases. For decoupled cloud cases, on the other hand, the PBLH blow~~
482 ~~clouds is sought to avoid cloud interference.~~ For coupled clouds, DTDS-derived PBLHs

483 show a strong correlation with RS-derived PBLHs with a correlation coefficient (R) of
484 ~ 0.9 ([Figure 10d](#)). For decoupled cases, the correlation between DTDS-derived PBLHs
485 and RS-derived PBLHd is generally good (R = 0.73) but worse than the correlation for
486 coupled cases ([Figure 10h](#)). ~~for a the~~As pointed out in previous studies (Chu et al., 2019;
487 Hageli et al., 2000; Lewis et al., 2013; Su et al., 2017b), it has been a persistent problem
488 to retrieve the PBLH under cloudy conditions since the ~~large-strong~~ backscattering and
489 step signals from cloud interference would be excluded to avoid interfering with the
490 retrievals. ~~With our method, T~~[the PBLH determined by our method under a cloudy](#)
491 ~~conditions demonstrates reasonably well accuracy is much more reasonable.~~

492 ~~Compared to the clear sky cases discussed in previous studies (e.g., Chu et al., 2019;~~
493 ~~Yang et al., 2017), the DTDS-derived PBLH shows a much higher correlation with RS-~~
494 ~~derived PBLH for coupled cloud cases and has a similar R as the RS-derived PBLH for~~

Formatted: Font: Not Bold

Formatted: Font: (Asian) Times New Roman, Bold, Font color: Black

Formatted: Font: Not Bold

Formatted: Indent: First line: 0.29"

Formatted: Font: Not Bold

Formatted: Font: Not Bold

Formatted: Font color: Auto

495 ~~decoupled cloud cases.~~ Moreover, due to the different definitions of the PBLH and
496 aerosol stratification within the PBL, there are always considerable differences between
497 lidar- and RS-derived PBLHs, which cannot be eliminated by a specific algorithm (Chu
498 et al., 2019; Su et al., 2020).

499

500 **5 Summary**

501 In this study, we proposed a novel method for distinguishing between coupled and
502 decoupled low clouds over land. Based on the understanding of PBL processes and
503 quantitative analyses, we developed a lidar-based method (DTDS) to identify the
504 coupling state of low clouds over the SGP site. In practice, we identified a coupled
505 cloud when the position of the cloud base was generally close to or lower than the
506 previous position of the PBL top, with the LCL serving as an additional restriction.
507 Compared to using the LCL alone, the coupled states identified by the DTDS method
508 show better consistency with the results derived from radiosondes, with about 10%
509 differences between the lidar-based retrievals and radiosonde results.

510 Not only coupled state, also retrieved by the method is the PBLH under cloudy
511 conditions. A long-lasting problem with lidar-retrieval of PBLH is either incapability
512 of retrieval or large uncertainties induced by the occurrence of low clouds (e.g., Chu et
513 al., 2019; Hageli et al., 2000; Lewis et al., 2013), we address this issue by separately
514 considering the coupled and decoupled of low clouds. Specifically, in coupled
515 conditions, the position of the coupled cloud serves as a good reference for identifying
516 the PBLH. In decoupled conditions, the large backscatter and step signals from clouds

517 would be excluded to avoid interfering with the retrievals. With our method, cloudy
518 conditions are well handled.

519 With the new method, we study the difference of cloud-PBL interactions in coupled
520 and decoupled conditions. In contrast to the sensitive responses of coupled clouds to
521 changes in the PBLH and buoyancy, the decoupled clouds and the PBLH are weakly
522 related. Due to their different relationships with the PBL, a robust distinguishment
523 between the coupled and decoupled low clouds is critical for further investigating the
524 coupled land-atmosphere system and aerosol-cloud interactions. Our methodology
525 paves a solid ground for such pursuits.

526

527 *Data availability.* All these datasets are publicly available at the ARM archive
528 https://adc.arm.gov/discovery/#/results/site_code::sgp. The products developed in this
529 study, i.e., cloud states and the PBLH, are currently available upon request from the
530 lead author (tianning@umd.edu) and are expected to be added to the ARM archive in
531 the near future.

532

533 *Author contribution.* T.S., Y.Z., and Z.L. conceptualized this study. T.S. carried out the
534 analysis, with comments from other co-authors. T.S., Y.Z., and Z.L. interpreted the data
535 and wrote the manuscript.

536

537 *Competing interests.* The authors declare that they have no conflict of interest.

538

539 *Acknowledgements.* This work was supported by grants from the U.S. Department of
540 Energy (DE-SC0018996), the National Science Foundation (AGS1837811), and NASA
541 (NNX16AN61G). We acknowledge the provision of radiosonde, MPL data, surface
542 meteorological data, and cloud products by the U.S. Department of Energy's ARM
543 program. [We thank the two anonymous reviewers for their comments.](#)

544

545 **References**

546 [Berkes, F., Hoor, P., Bozem, H., Kunkel, D., Sprenger, M. and Henne, S. \(2016\).
547 *Airborne observation of mixing across the entrainment zone during PARADE 2011.*
548 *Atmospheric Chemistry and Physics*, 16\(10\), pp.6011-6025.](#)

549 Betts, A.K. (2009). Land-surface-atmosphere coupling in observations and models.
550 *Journal of Advances in Modeling Earth Systems*, 1(3).
551 <https://doi.org/10.3894/JAMES.2009.1.4>

552 Bretherton, C. S., [and](#) Wyant, M. C. (1997). Moisture transport, lower-tropospheric
553 stability, and decoupling of cloud-topped boundary layers. *Journal of the*
554 *Atmospheric Sciences*, 54(1), 148–167. [https://doi.org/10.1175/1520-](https://doi.org/10.1175/1520-0469(1997)054<0148:MTL TSA>2.0.CO;2)
555 [0469\(1997\)054<0148:MTL TSA>2.0.CO;2](https://doi.org/10.1175/1520-0469(1997)054<0148:MTL TSA>2.0.CO;2)

556 Brooks, I. M. (2003). Finding boundary layer top: application of a wavelet covariance

557 transform to lidar backscatter profiles. *Journal of Atmospheric and Oceanic*
558 *Technology*, 20, 1092–1105. [https://doi.org/10.1175/1520-](https://doi.org/10.1175/1520-0426(2003)020<1092:FBLTAO>2.0.CO;2)
559 [0426\(2003\)020<1092:FBLTAO>2.0.CO;2](https://doi.org/10.1175/1520-0426(2003)020<1092:FBLTAO>2.0.CO;2)

560 Campbell, J. R., Hlavka, D. L., Welton, E. J., Flynn, C. J., Turner, D. D., Spinhirne, J.
561 D., ... Hwang, I. H. (2002). Full-time, eye-safe cloud and aerosol lidar
562 observation at atmospheric radiation measurement program sites: instruments and
563 data processing. *Journal of Atmospheric and Oceanic Technology*, 19(4), 431–442.
564 [https://doi.org/10.1175/1520-0426\(2002\)019<0431:FTESCA>2.0.CO;2](https://doi.org/10.1175/1520-0426(2002)019<0431:FTESCA>2.0.CO;2)

565 Campbell, J.R., Welton, E.J., Spinhirne, J.D., Ji, Q., Tsay, S.C., Piketh, S.J., Barenbrug,
566 M. and Holben, B.N., 2003. Micropulse lidar observations of tropospheric aerosols
567 over northeastern South Africa during the ARREX and SAFARI 2000 dry season
568 experiments. *Journal of Geophysical Research: Atmospheres*, 108(D13).

569 Cheruy, F., Dufresne, J. L., Hourdin, F., & Ducharne, A. (2014). Role of clouds and
570 land-atmosphere coupling in midlatitude continental summer warm biases and
571 climate change amplification in CMIP5 simulations. *Geophysical Research Letters*,
572 41(18), 6493–6500. <https://doi.org/10.1002/2014GL061145>

573 Chu, Y., Li, J., Li, C., Tan, W., Su, T., & Li, J. (2019). Seasonal and diurnal
574 variability of planetary boundary layer height in Beijing: intercomparison between
575 MPL and WRF results. *Atmospheric Research*, 227, 1–13.
576 <https://doi.org/10.1016/j.atmosres.2019.04.017>

577 Clothiaux, E. E., Ackerman, T. P., Mace, G. G., Moran, K. P., Marchand, R. T., Miller,

578 M. A., & Martner, B. E. (2000). Objective determination of cloud heights and
579 radar reflectivities using a combination of active remote sensors at the ARM CART
580 sites. *Journal of Applied Meteorology*, 39(5), 645–665.
581 [https://doi.org/10.1175/1520-0450\(2000\)039<0645:ODOCHA>2.0.CO;2](https://doi.org/10.1175/1520-0450(2000)039<0645:ODOCHA>2.0.CO;2)

582 [Cromwell, E., and Flynn, D. \(2019\). Lidar cloud detection with fully convolutional
583 networks. In 2019 IEEE Winter Conference on Applications of Computer Vision
584 \(WACV\) \(pp. 619-627\). IEEE.](#)

585 [de Roode, S.R. and Wang, Q. \(2007\). Do stratocumulus clouds detrain? FIRE I data
586 revisited. *Boundary-layer meteorology*, 122\(2\), pp.479-491.](#)

587 Demoz, B., Flamant, C., Weckwerth, T., Whiteman, D., Evans, K., Fabry, F., &
588 Schwemmer, G. (2006). The dryline on 22 May 2002 during IHOP_2002:
589 convective-scale measurements at the profiling site. *Monthly Weather Review*,
590 134(1), 294–310. <https://doi.org/10.1175/MWR3054.1>

591 Dong, X., Schwantes, A. C., Xi, B., & Wu, P. (2015). Investigation of the marine
592 boundary layer cloud and CCN properties under coupled and decoupled conditions
593 over the Azores. *Journal of Geophysical Research: Atmospheres*, 120, 6179–6191.
594 <https://doi.org/10.1002/2014JD022939>

595 Driedonks, A. G. M. (1982). Models and observations of the growth of the atmospheric
596 boundary layer. *Boundary-Layer Meteorology*, 23(3), 283–306.
597 <https://doi.org/10.1007/BF00121117>

598 Ek, M. B., & Holtslag, A. A. M. (2004). Influence of soil moisture on boundary

599 layer cloud development. *Journal of Hydrometeorology*, 5(1), 86–99.
600 [https://doi.org/10.1175/1525-7541\(2004\)005<0086:IOSMOB>2.0.CO;2](https://doi.org/10.1175/1525-7541(2004)005<0086:IOSMOB>2.0.CO;2)

601 Flynn, D., Shi, Y., Lim, K., & Riihimaki, L. (2017). Cloud Type Classification
602 (cldtype) Value-Added Product. Ed. by Robert Stafford, ARM Research Facility.
603 DOE/SC-ARM-TR-200.

604 Garratt, J. R. (1994). Review: the atmospheric boundary layer. *Earth-Science Reviews*,
605 37(1-2), 89–134. [https://doi.org/10.1016/0012-8252\(94\)90026-4](https://doi.org/10.1016/0012-8252(94)90026-4)

606 Glenn, I. B., Feingold, G., Gristey, J. J., & Yamaguchi, T. (2020). Quantification of
607 the radiative effect of aerosol-cloud-interactions in shallow continental cumulus
608 clouds. *Journal of the Atmospheric Sciences*, 77, 2905–2920.
609 <https://doi.org/10.1175/JAS-D-19-0269.1>

610 Golaz, J. C., Larson, V. E., & Cotton, W. R. (2002). A PDF-based model for
611 boundary layer clouds. Part I: Method and model description. *Journal of the*
612 *Atmospheric Sciences*, 59(24), 3540–3551. [https://doi.org/10.1175/1520-0469\(2002\)059<3540:APBMFB>2.0.CO;2](https://doi.org/10.1175/1520-0469(2002)059<3540:APBMFB>2.0.CO;2)

614 Guo, J., Miao, Y., Zhang, Y., Liu, H., Li, Z., Zhang, W., ... Zhai, P. (2016). The
615 climatology of planetary boundary layer height in China derived from radiosonde
616 and reanalysis data. *Atmospheric Chemistry and Physics*, 16(20), 13,309–13,319.
617 <https://doi.org/10.5194/acp-16-13309-2016>

618 Hageli, P., Steyn, D. G., & Strawbridge, K. B. (2000). Spatial and temporal
619 variability of mixed-layer depth and entrainment zone thickness. *Boundary-Layer*

620 *Meteorology*, 97, 47–71. <https://doi.org/10.1023/A:1002790424133>

621 Holdridge, D., Ritsche, M., Prell, J., & Coulter, R. (2011). Balloon-borne sounding
622 system (SONDE) handbook. <https://www.arm.gov/capabilities/instruments/sonde>

623 [Holzworth, G. C., \(1964\). Estimates of mean maximum mixing depths in the contiguous](#)
624 [United States. Mon. Weather Rev., 92, 235–242. https://doi.org/10.1175/1520-](#)
625 [0493\(1964\)092<0235:eommmmd>2.3.co:2.](#)

626 Jones, C., Bretherton, C., & Leon, D. (2011). Coupled vs. decoupled boundary
627 layers in VOCALS-REx. *Atmospheric Chemistry and Physics*, 11(14), 7143–7153.
628 <https://doi.org/10.5194/acp-11-7143-2011>

629 Kasahara, A. (1974). Various vertical coordinate systems used for numerical weather
630 prediction. *Monthly Weather Review*, 102(7), 509–522.
631 [https://doi.org/10.1175/1520-0493\(1974\)102<0509:VVCSUF>2.0.CO:2](https://doi.org/10.1175/1520-0493(1974)102<0509:VVCSUF>2.0.CO:2)

632 Lewis, J. R., Welton, E. J., Molod, A. M., & Joseph, E. (2013). Improved boundary
633 layer depth retrievals from MPLNET. *Journal of Geophysical Research:*
634 *Atmospheres*, 118(17), 9870–9879. <https://doi.org/10.1002/jgrd.50570>

635 [Lim, K.S.S., Riihimaki, L.D., Shi, Y., Flynn, D., Kleiss, J.M., Berg, L.K., Gustafson,](#)
636 [W.I., Zhang, Y. and Johnson, K.L. \(2019\). Long-term retrievals of cloud type and](#)
637 [fair-weather shallow cumulus events at the ARM SGP site. Journal of Atmospheric](#)
638 [and Oceanic Technology, 36\(10\), pp.2031-2043.](#)

639 Liu, S. Y., & Liang, X. Z. (2010). Observed diurnal cycle climatology of planetary

640 boundary layer height. *Journal of Climate*, 23, 5790–5809.

641 <https://doi.org/10.1175/2010JCLI3552.1>

642 [Lock, A. P., Brown, A. R., Bush, M. R., Martin, G. M., & Smith, R. N. B. \(2000\). A](#)
643 [new boundary layer mixing scheme. Part I: Scheme description and single-column](#)
644 [model tests. *Monthly weather review*, 128\(9\), 3187-3199.](#)

645 Nicholls, S. (1984). The dynamics of stratocumulus: aircraft observations and
646 comparisons with a mixed layer model. *Quarterly Journal of the Royal*
647 *Meteorological Society*, 110(466), 783–820.
648 <https://doi.org/10.1002/qj.49711046603>

649 [Ott, L. E., Bacmeister, J., Pawson, S., Pickering, K., Stenchikov, G., Suarez, M., ... and](#)
650 [Xueref-Remy, I. \(2009\). Analysis of convective transport and parameter sensitivity](#)
651 [in a single column version of the Goddard earth observation system, version 5,](#)
652 [general circulation model. *Journal of the Atmospheric Sciences*, 66\(3\), 627-646.](#)

653 Platt, C. M., Young, S. A., Carswell, A. I., Pal, S. R., McCormick, M. P., Winker, D.
654 M., ... [and](#) Wooldridge, C. (1994). The Experimental Cloud Lidar Pilot Study
655 (ECLIPS) for cloud-radiation research. *Bulletin of the American Meteorological*
656 *Society*, 75, 1635–1654. [https://doi.org/10.1175/1520-](https://doi.org/10.1175/1520-0477(1994)075<1635:TECLPS>2.0.CO;2)
657 [0477\(1994\)075<1635:TECLPS>2.0.CO;2](#)

658 Revercomb, H.E., Turner, D.D., Tobin, D.C., Knuteson, R.O., Feltz, W.F., Barnard, J.,
659 Bösenberg, J., Clough, S., Cook, D., Ferrare, R. and Goldsmith, J., 2003. The ARM
660 program's water vapor intensive observation periods: Overview, initial

661 accomplishments, and future challenges. *Bulletin of the American Meteorological*
662 *Society*, 84(2), pp.217-236.

663 Romps, D. M. (2017). Exact expression for the lifting condensation level. *Journal of*
664 *the Atmospheric Sciences*, 74(12), 3891–3900. [https://doi.org/10.1175/JAS-D-17-](https://doi.org/10.1175/JAS-D-17-0102.1)
665 [0102.1](https://doi.org/10.1175/JAS-D-17-0102.1)

666 Santanello Jr., J. A., Dirmeyer, P. A., Ferguson, C. R., Findell, K. L., Tawfik, A. B.,
667 Berg, A., ... & Roundy, J. (2018). Land–atmosphere interactions: the LoCo
668 perspective. *Bulletin of the American Meteorological Society*, 99(6), 1253–1272.
669 <https://doi.org/10.1175/BAMS-D-17-0001.1>

670 Sawyer, V., & Li, Z. Q. (2013). Detection, variations and intercomparison of the
671 planetary boundary layer depth from radiosonde, lidar and infrared spectrometer.
672 *Atmospheric Environment*, 79, 518–528.
673 <https://doi.org/10.1016/j.atmosenv.2013.07.019>

674 [Seidel, D. J., Ao, C. O., and Li, K. \(2010\). Estimating climatological planetary boundary layer](#)
675 [heights from radiosonde observations: Comparison of methods and uncertainty analysis.](#)
676 [Journal of Geophysical Research: Atmospheres](#), 115(D16).

677 [Silber, I., J. Verlinde, E. W. Eloranta, C. J. Flynn, and D. M. Flynn \(2018\), Polar liquid](#)
678 [cloud base detection algorithms for high spectral resolution or micropulse lidar data.](#)
679 [J. Geophys. Res.: Atmos.](#), doi: 10.1029/2017JD027840.

680 [Storer, R.L., Griffin, B.M., Höft, J., Weber, J.K., Raut, E., Larson, V.E., Wang, M. and](#)
681 [Rasch, P.J. \(2015\). Parameterizing deep convection using the assumed probability](#)

Formatted: Default Paragraph Font, Font: 11 pt, Font color: Text 1

Formatted: Default Paragraph Font, Font: 11 pt, Font color: Text 1

682 [density function method. Geoscientific Model Development, 8\(1\), pp.1-19.](#)

683 Stull, R. B. (1988). *An Introduction to Boundary Layer Meteorology*. Dordrecht:
684 Springer Netherlands.

685 Su, T., Li, J., Li, C. C., Xiang, P. Z., Lau, A. K. H., Guo, J. P., ... [and](#) Miao, Y. C.
686 (2017b). An intercomparison of long-term planetary boundary layer heights
687 retrieved from CALIPSO, ground-based lidar, and radiosonde measurements over
688 Hong Kong. *Journal of Geophysical Research: Atmospheres*, 122, 3929–3943.
689 <https://doi.org/10.1002/2016JD025937>

690 Su, T., Li, J., Li, J., Li, C., Chu, Y., Zhao, Y., ... Wang, L. (2017a). The evolution of
691 springtime water vapor over Beijing observed by a high dynamic Raman lidar
692 system: case studies. *IEEE Journal of Selected Topics in Applied Earth
693 Observations and Remote Sensing*, 10(5), 1715–1726.
694 <https://doi.org/10.1109/JSTARS.2017.2653811>

695 Su, T., Li, Z., [and](#) Kahn, R. (2018). Relationships between the planetary boundary
696 layer height and surface pollutants derived from lidar observations over China:
697 regional pattern and influencing factors. *Atmospheric Chemistry and Physics*,
698 18(21), 15,921–15,935. <https://doi.org/10.5194/acp-18-15921-2018>

699 Su, T., Li, Z., [and](#) Kahn, R. (2020). A new method to retrieve the diurnal variability
700 of planetary boundary layer height from lidar under different thermodynamic
701 stability conditions. *Remote Sensing of Environment*, 237, 111519.
702 <https://doi.org/10.1016/j.rse.2019.111519>

- 703 Teixeira, J., [and](#) Hogan, T. F. (2002). Boundary layer clouds in a global atmospheric
704 model: simple cloud cover parameterizations. *Journal of Climate*, 15(11), 1261–
705 1276. [https://doi.org/10.1175/1520-
706 0442\(2002\)015<1261:BLCIAG>2.0.CO;2](https://doi.org/10.1175/1520-0442(2002)015<1261:BLCIAG>2.0.CO;2);Vogelezang, D. H. P., and Holtslag, A. A.
707 M. (1996). Evaluation and model impacts of alternative boundary-layer height
708 formulations. *Boundary-Layer Meteorology*, 81(3-4), 245–269.
709 <https://doi.org/10.1007/BF02430331>
- 710 Wallace, J. M., [and](#) Hobbs, P. V. (2006). *Atmospheric Science: an Introductory Survey*.
711 Amsterdam, Boston: Elsevier Academic Press.
- 712 Warren, G., Hahn, C. J., London, J., Chervin, M., [and](#) Jenne, R. L. (1986). Global
713 distribution of total cloud cover and cloud type amounts over land. (Rep. DOE/ER-
714 0406). Washington, DC: U.S. DOE Office of Energy Research.
- 715 Wei, J., Huang, W., Li, Z., Sun, L., Zhu, X., Yuan, Q., Liu, L. and Cribb, M., 2020.
716 Cloud detection for Landsat imagery by combining the random forest and
717 superpixels extracted via energy-driven sampling segmentation approaches.
718 *Remote Sensing of Environment*, 248, p.112005.
- 719 Welton, E. J., Campbell, J. R., Spinhirne, J. D., [and](#) Scott III, V. S. (2001). Global
720 monitoring of clouds and aerosols using a network of micropulse lidar systems. In
721 *Lidar Remote Sensing for Industry and Environment Monitoring* (Vol. 4153, 151–
722 158). International Society for Optics and Photonics.
- 723 Wu, X., Grabowski, W. W., [and](#) Moncrieff, M. W. (1998). Long-term behavior of cloud

724 systems in TOGA COARE and their interactions with radiative and surface
725 processes. Part I: Two-dimensional modeling study. *Journal of the Atmospheric*
726 *Sciences*, 55(17), 2693–2714. [https://doi.org/10.1175/1520-](https://doi.org/10.1175/1520-0469(1998)055<2693:LTBOCS>2.0.CO;2)
727 [0469\(1998\)055<2693:LTBOCS>2.0.CO;2](https://doi.org/10.1175/1520-0469(1998)055<2693:LTBOCS>2.0.CO;2)

728 Yang, D., Li, C., Lau, A. K. H., & Li, Y. (2013). Long-term measurement of daytime
729 atmospheric mixing layer height over Hong Kong. *Journal of Geophysical*
730 *Research: Atmospheres*, 118(5), 2422–2433. <https://doi.org/10.1002/jgrd.50251>

731 Yang, T., Wang, Z., Zhang, W., Gbaguidi, A., Sugimoto, N., Wang, X., Matsui, I. and
732 Sun, Y., 2017. Boundary layer height determination from lidar for improving air
733 pollution episode modeling: development of new algorithm and evaluation.
734 *Atmospheric Chemistry and Physics*, 17(10), p.6215.

735 Zhao, C., Wang, Y., Wang, Q., Li, Z., Wang, Z., & Liu, D. (2014). A new cloud and
736 aerosol layer detection method based on micropulse lidar measurements. *Journal*
737 *of Geophysical Research: Atmospheres*, 119(11), 6788–6802.
738 <https://doi.org/10.1002/2014JD021760>

739 Zheng, Y., & Li, Z. (2019). Episodes of warm-air advection causing cloud-surface
740 decoupling during the MARCUS. *Journal of Geophysical Research: Atmospheres*,
741 124(22). <https://doi.org/10.1029/2019JD030835>

742 Zheng, Y., & Rosenfeld, D. (2015). Linear relation between convective cloud base
743 height and updrafts and application to satellite retrievals. *Geophysical Research*
744 *Letters*, 42(15), 6485–6491. <https://doi.org/10.1002/2015GL064809>

745 Zheng, Y., Rosenfeld, D., [and](#) Li, Z. (2018). Estimating the decoupling degree of
746 subtropical marine stratocumulus decks from satellite. *Geophysical Research*
747 *Letters*, 45. <https://doi.org/10.1029/2018GL078382>

748 Zheng, Y., Sakradzija, M., Lee, S.-S., [and](#) Li, Z. (2020). Theoretical understanding of
749 the linear relationship between convective updrafts and cloud-base height for
750 shallow cumulus clouds. Part II: Continental conditions. *Journal of the*
751 *Atmospheric Sciences*, 77, 1313–1328. <https://doi.org/10.1175/JAS-D-19-0301.1>

752

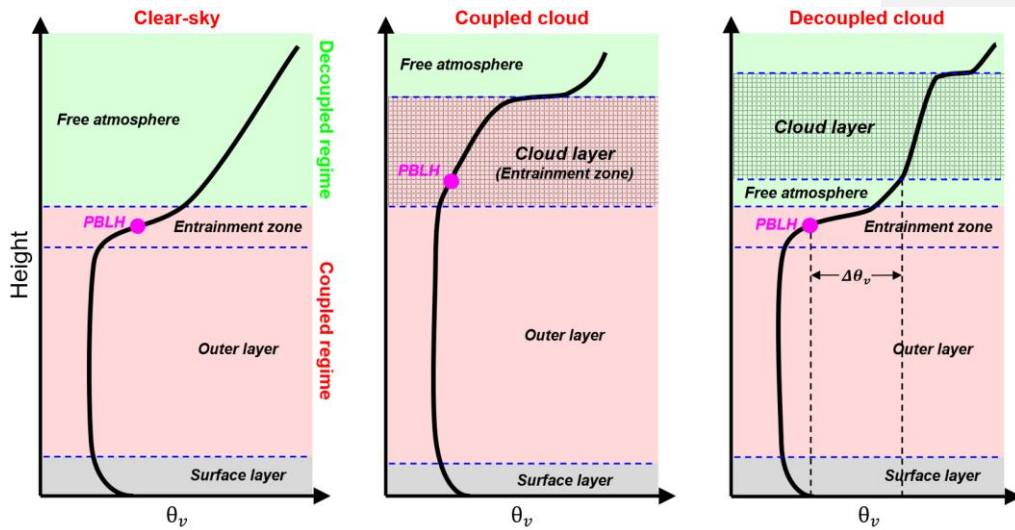
753 **Tables**

754 **Table 1.** List of parameters in the flow chart of DTDS (Figure 54). These parameters
 755 are related with three factors, including LCL, PBLH, CBH. The sensitivity of selection
 756 of these parameters is presented. The detailed impacts of variations in these parameters
 757 on the retrievals of cloud coupling and PBLH are presented in Figure 7-6 and Figure
 758 87, respectively.

759

	Unit	Related factors	Value	Sensitivity (coupled states)	Sensitivity ⁷⁶⁰ (PBLH)
A₁	km	LCL / PBLH	0.7	Low	Low
A₂	km	PBLH	0.2	High	Low
A₃	km	LCL	0.15	Low	Low
A₄	dimensionless	CBH	1.35	Low	Low
A₅	dimensionless	CBH	1.1	Low	High

761 **Figures**

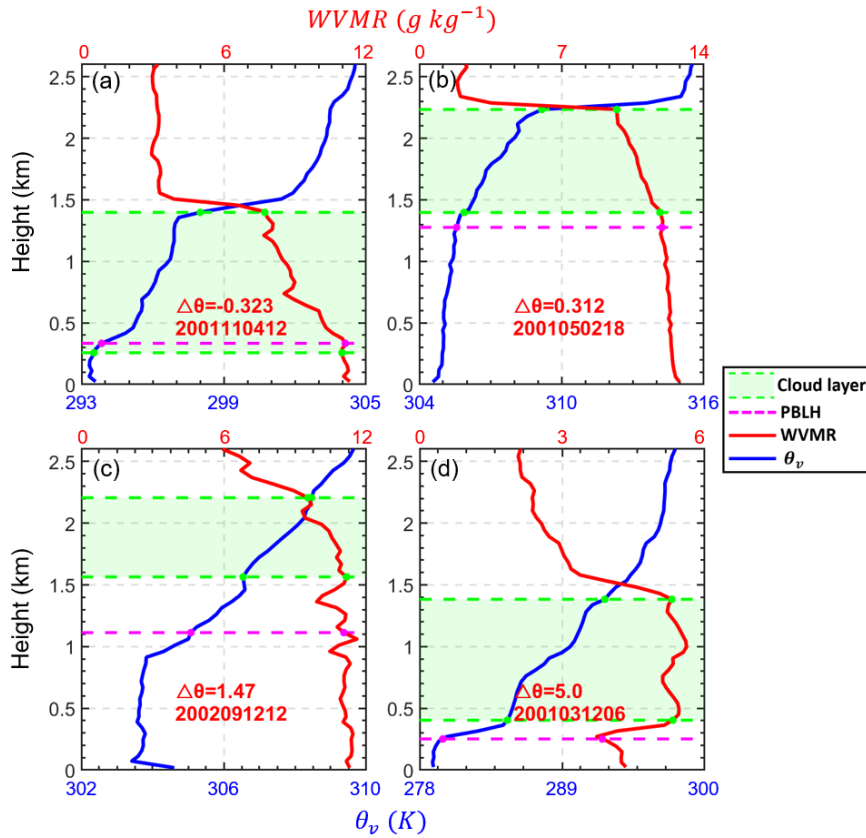


762

763 **Figure 1.** Idealized vertical profiles of virtual potential temperature (θ_v) under the clear-
764 sky, coupled cloud, and decoupled cloud over land. The surface layer, outer layer
765 entrainment zone, and free atmosphere are divided by the blue dash lines. The cloudy
766 layer is marked as the shaded area, and PBLH is marked as the pink point. Red and
767 green zones indicate the coupled and decoupled regime, respectively. Elements (e.g.,
768 turbulence, heat fluxes, cloud) in the coupled regime are directly affected by the PBL
769 processes, while these elements are not directly affected by the PBL processes in the
770 decoupled regime. For the coupled cases, the cloud base is below the capping inversion
771 of entrainment zone. For the decoupled cases, the cloud base is above the capping
772 inversion.

773

774

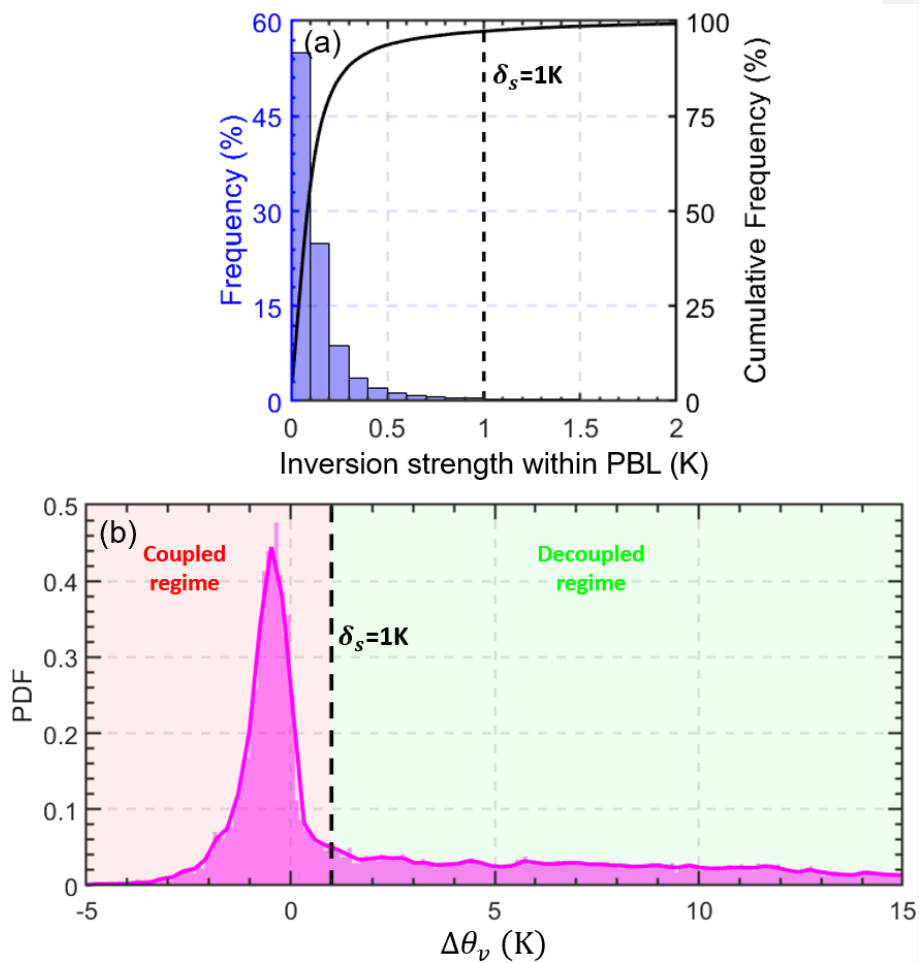


775

776 **Figure 2.** Virtual potential temperature (θ_v , red lines) and water vapor mixing ratio
 777 (WVMR, blue lines) profiles from radiosonde (RS) over the Southern Great Plains site
 778 for different cases. The differences in virtual potential temperature between the cloud
 779 base and the planetary boundary layer (PBL) top are expressed as $\Delta\theta_v$ ($\theta_v^{\text{CBH}} -$
 780 θ_v^{PBLH}). The time of each radiosonde launch is marked in each panel as
 781 “YYYYMMDDHH”, where YYYY, MM, DD, and HH indicates the year, month, day,
 782 and local time, respectively. Green regions are cloud layers, and green dashed lines
 783 indicate their boundaries. ~~PBL heights are~~ The cloud layer is obtained from the

784 [CLDTYPE/ARSCL data](#). PBLHs is derived from RS data, and is marked as dashed pink

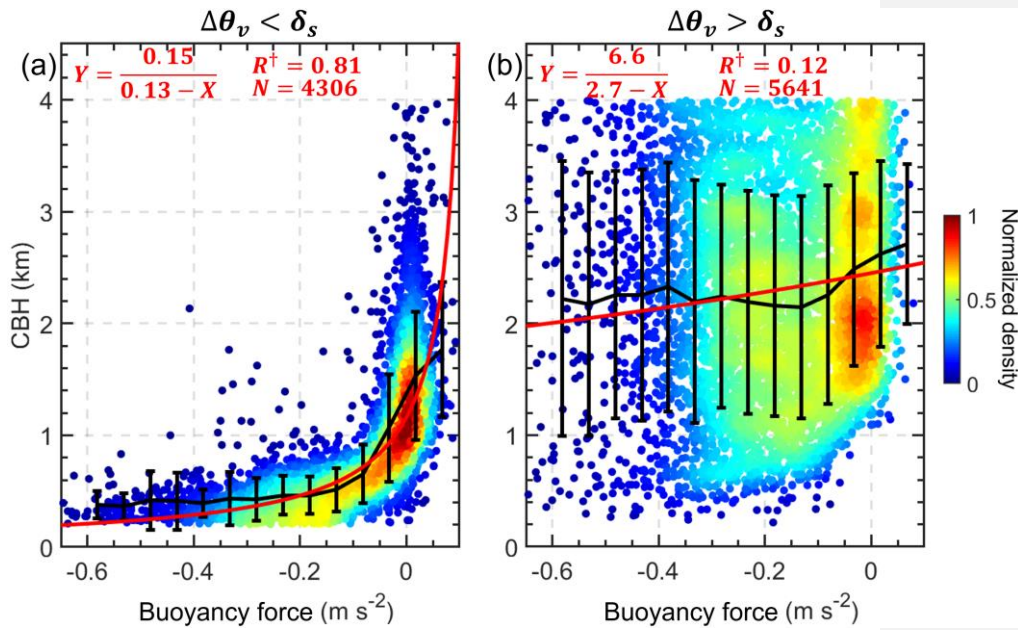
785 lines.



786

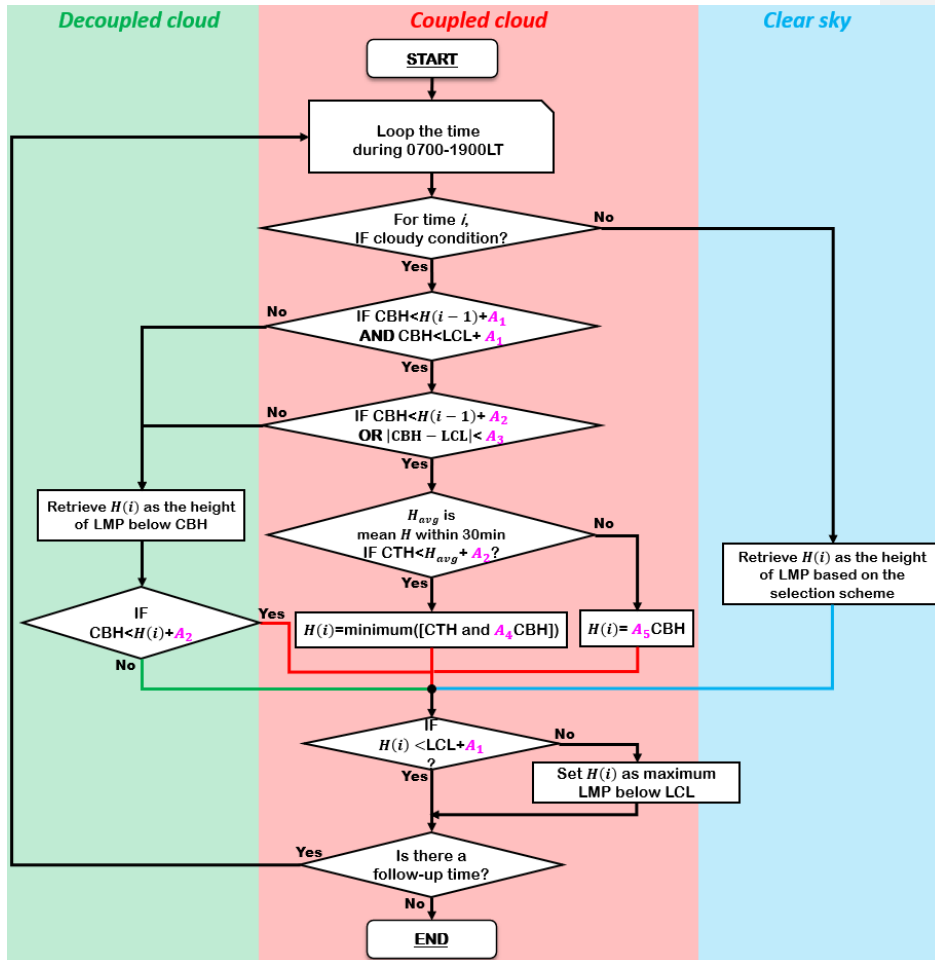
787 **Figure 3.** (a) Blue bars represent the inversion strength of θ_v within the PBL. The
788 inversion strength is derived from the radiosonde during daytime (0800-1900LT). The
789 inversions near surface or across PBL top are excluded. The black solid line represents
790 cumulative frequency. (b) Pink area represents the probability density function (PDF)
791 of the differences in the virtual potential temperature between cloud-base height (CBH)

792 and PBLH ($\Delta\theta_v = \theta_v^{\text{CBH}} - \theta_v^{\text{PBLH}}$). By using a threshold of δ_s (1 K), coupled and
 793 decoupled regimes are classified.



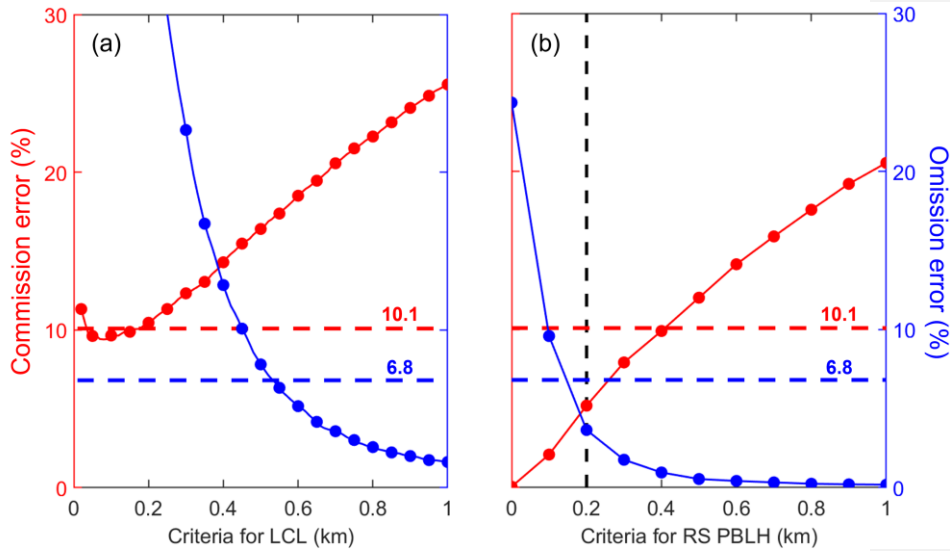
794

795 **Figure 4.** The relationships between cloud base height (CBH) and buoyancy forces in
 796 the lower atmosphere (0–1 km) for (a) $\Delta\theta_v < \delta_s$ and (b) $\Delta\theta_v > \delta_s$. $\Delta\theta_v$ represents the
 797 differences in the virtual-potential temperature (θ_v) between CBH and PBLH. Black
 798 lines represent the mean values in each bin, and the whiskers indicate the standard
 799 deviations. Red lines represent the inverse fits. The fitting functions and number of
 800 samples (N) are given in each panel, along with the correlation coefficient (R^2) for the
 801 inverse fit.



802

803 **Figure 54.** The flow chart of the updated DTDS algorithm. In this diagram, $H(i)$ is
 804 the retrieved planetary boundary layer height (PBLH) at time i . CBH and CTH represent
 805 the base and top heights, respectively, of the lowest cloud at time i . The PBLH part for
 806 selecting the suitable local maximum position (LMP) follows Su et al. (2020), and a
 807 detailed scheme for identifying a coupled cloud is added to the DTDS algorithm. LCL
 808 stands for lifted condensation level. Five empirical parameters (A_1, A_2, A_3, A_4, A_5) are
 809 set as 0.7, 0.2, 0.15, 1.35, 1.1, respectively.



810

811

812

813

814

815

816

817

818

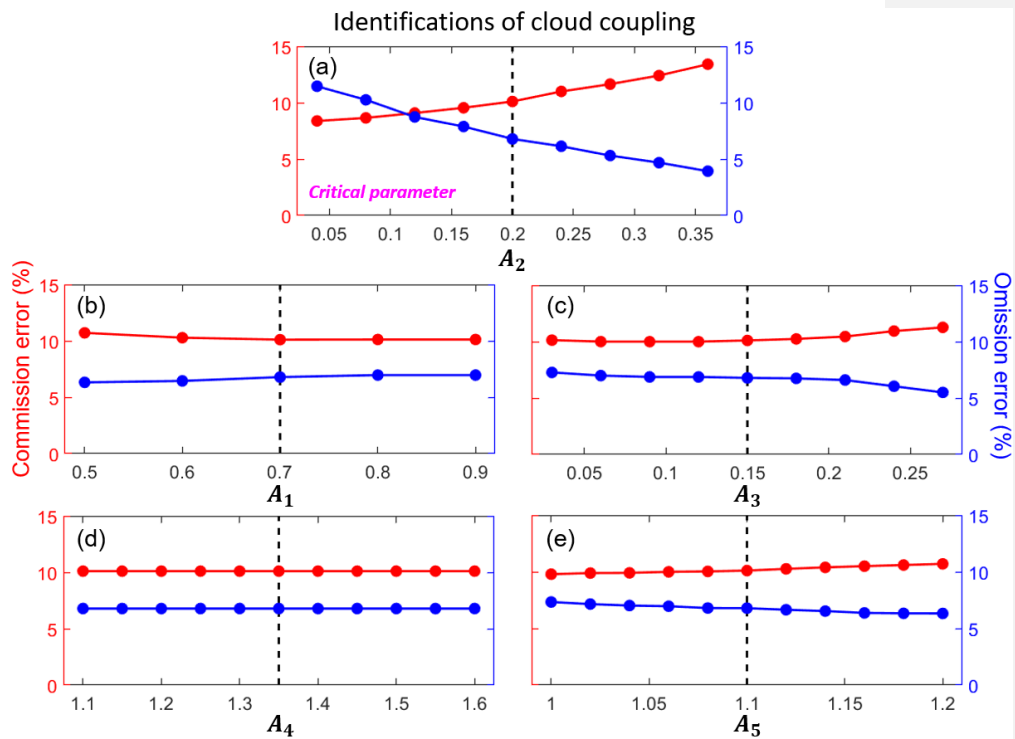
819

820

821

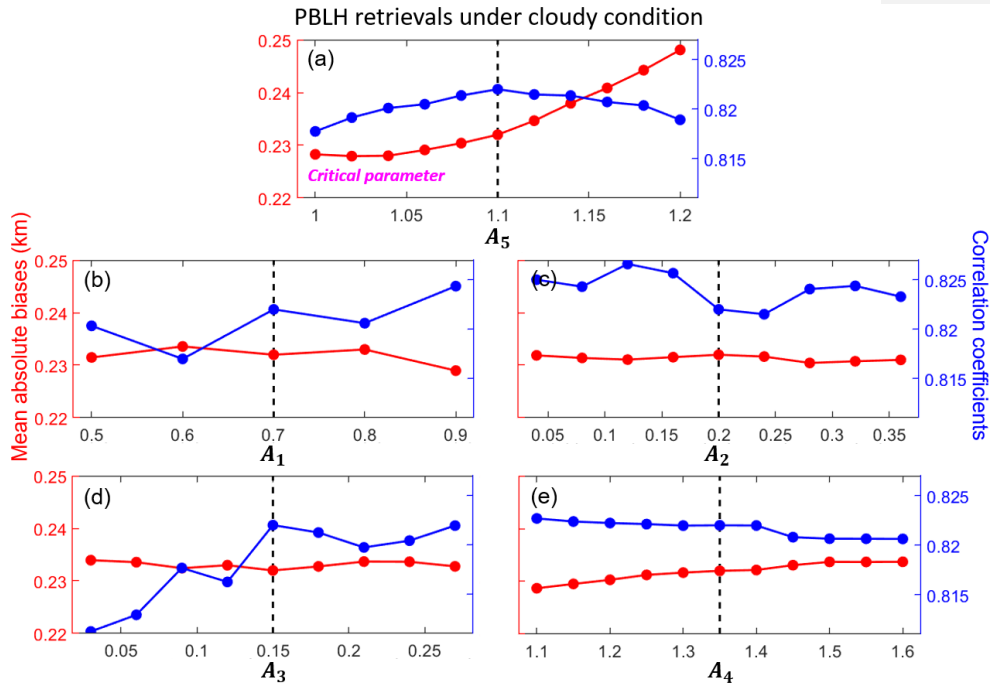
822

Figure 65. Commission errors and omission errors of coupled cloud identifications (a) for different criteria for the lifted condensation level (LCL) and (b) for different criteria for the planetary boundary layer height (PBLH). “Criteria for LCL” means coupled clouds are identified if $|CBH - LCL| < \text{Criteria for LCL}$. Similarly, “Criteria for RS PBLH” means coupled clouds are identified if $CBH - RS \text{ PBLH} < \text{Criteria for RS PBLH}$. The red and blue dashed lines indicate the commission and omission errors, respectively, for the DTDS algorithm. CBH stands for cloud-base height, and RS stands for radiosonde. [By using ~7500 RS profiles, the cloud coupling state derived from the virtual potential temperature method \(Section 3.1\) is considered as the ground truth for evaluation.](#)



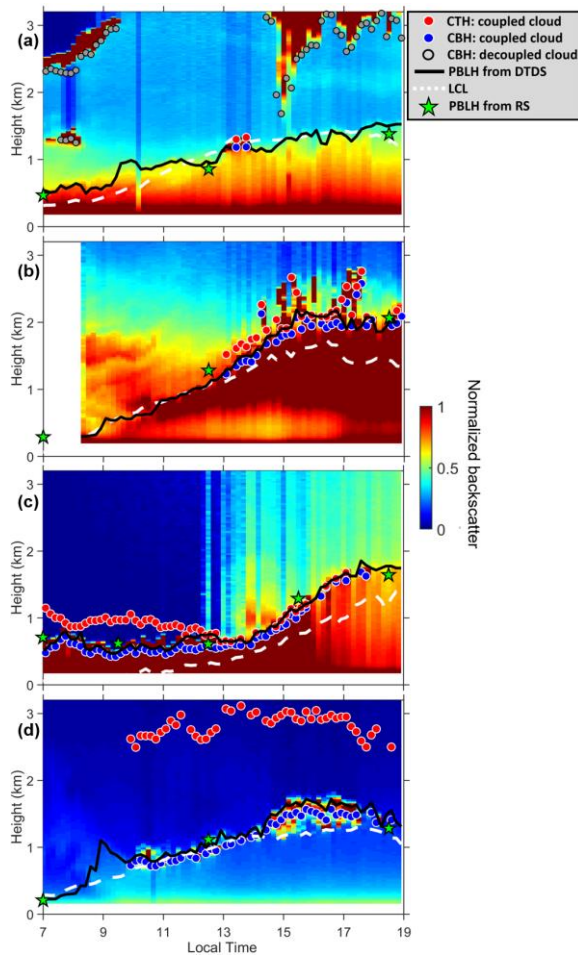
825

826 **Figure 76.** Commission errors (red line) and omission errors (blue line) of coupled
 827 cloud identifications for selecting different values of empirical parameters
 828 (A_1, A_2, A_3, A_4, A_5) in the DTDS algorithm. Black dash lines indicate the default values.
 829 For each test, one parameter is variable, while other parameters are set as default values.
 830 For identifications of cloud coupling, A_2 is the critical parameter.



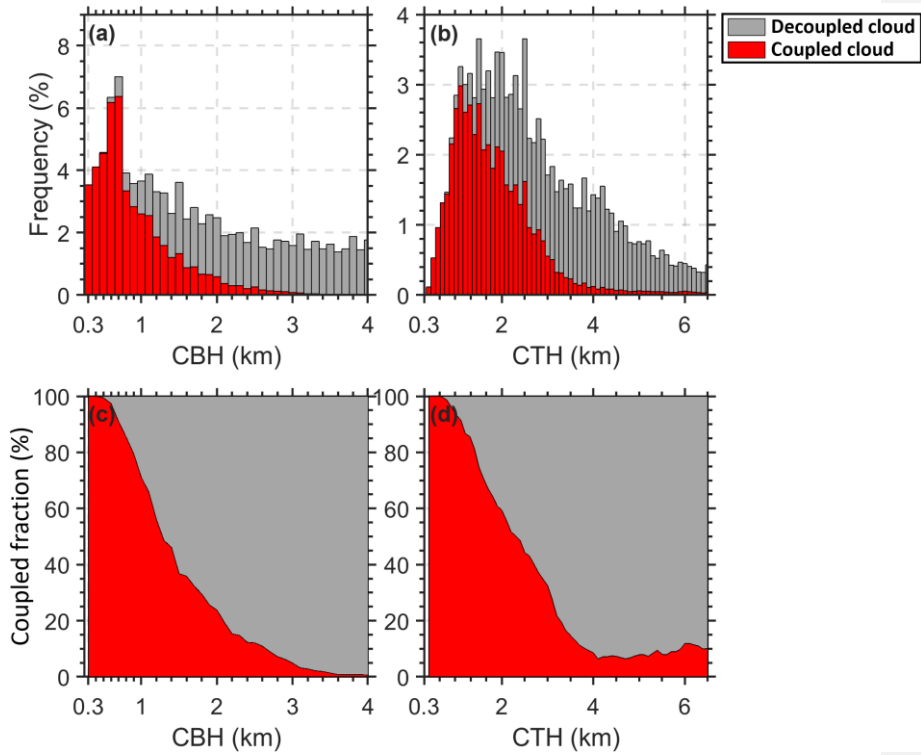
831

832 **Figure 87.** Red lines indicate the mean absolute biases between PBLH derived from
 833 lidar and radiosonde for selecting different values of empirical parameters
 834 (A_1, A_2, A_3, A_4, A_5) in the DTDS algorithm. Here, we only analyze the low cloud cases.
 835 Blue lines indicate the corresponding correlation coefficients between PBLH derived
 836 from lidar and radiosonde. Black dash lines indicate the default values. For each test,
 837 one parameter is variable, while other parameters are set as default values. For PBLH
 838 retrievals under cloudy conditions, A_5 is the critical parameter.



839

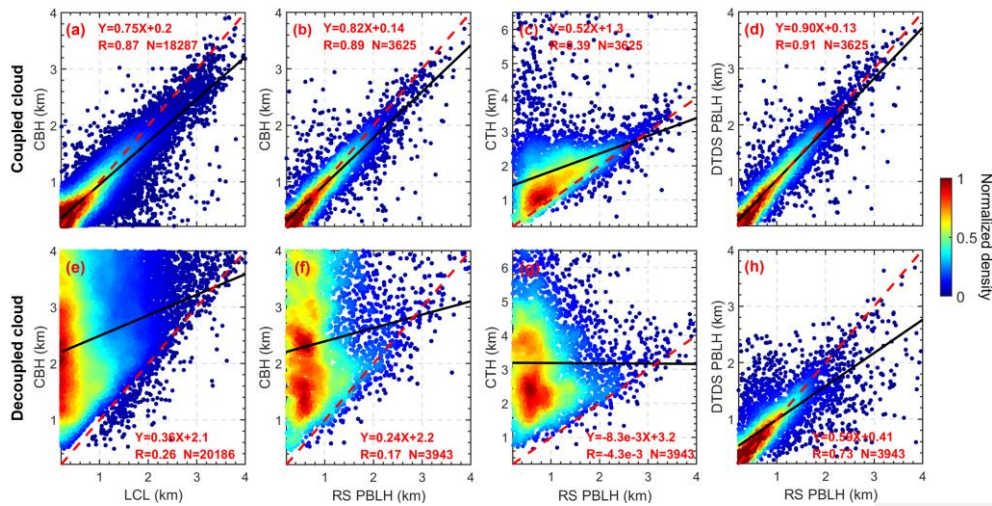
840 **Figure 98.** Daily backscatter profiles: (a) short-lived coupled cloud, (b) developed
 841 coupled cloud, (c) daylong coupled cloud, and (d) active coupled cloud. Backscatter is
 842 normalized to a range of 0–1 in arbitrary units. Red dots and blue dots indicate cloud-
 843 top heights (CTHs) and cloud-base heights (CBHs) of coupled clouds. Grey dots mark
 844 CBHs for decoupled clouds. Black lines and green stars mark the planetary boundary
 845 layer height (PBLH) retrieved from the DTDS algorithm and from radiosonde (RS)
 846 soundings, respectively. White dashed lines represent lifted condensation levels (LCLs).



847

848 **Figure 109.** The height-dependent occurrence frequencies of (a) the cloud-base height
 849 (CBH) and (b) the cloud-top height (CTH) for coupled clouds (red bars) and decoupled
 850 clouds (grey bars). The relative occurrence frequencies of (c) the CBH and (d) the CTH
 851 for coupled clouds (red area) and decoupled clouds (grey area).

852



853

854 **Figure 410.** The relationships between (a) LCL and CBH, (b) CBH and RS-derived
 855 PBLH, (c) CTH and RS-derived PBLH for coupled clouds, and (d) DTDS-derived
 856 PBLH and RS-derived PBLH. Panels (e-h) are similar to panels (a-d) but for decoupled
 857 clouds. Black lines represent the linear regressions. The linear fitting functions,
 858 correlation coefficients (R), and sampling numbers (N) are given in each panel.